

A Numerical Study on Toppling Failure of a Jointed Rock Slope by Using the Distinct Lattice Spring Model

Ji-Jian Lian¹ · Qin Li¹ · Xi-Fei Deng² · Gao-Feng Zhao¹ · Zu-Yu Chen^{3,4}

Received: 5 April 2017 / Accepted: 12 September 2017 / Published online: 21 September 2017
© Springer-Verlag GmbH Austria 2017

Abstract In this work, toppling failure of a jointed rock slope is studied by using the distinct lattice spring model (DLSM). The gravity increase method (GIM) with a sub-step loading scheme is implemented in the DLSM to mimic the loading conditions of a centrifuge test. A classical centrifuge test for a jointed rock slope, previously simulated by the finite element method and the discrete element model, is simulated by using the GIM-DLSM. Reasonable boundary conditions are obtained through detailed comparisons among existing numerical solutions with experimental records. With calibrated boundary conditions, the influences of the tensional strength of the rock block, cohesion and friction angles of the joints, as well as the spacing and inclination angles of the joints, on the flexural toppling failure of the jointed rock slope are investigated by using the GIM-DLSM, leading to some insight into evaluating the state of flexural toppling failure for a jointed slope and effectively preventing the flexural toppling failure of jointed rock slopes.

Keywords Toppling failure · Jointed rock slope · Distinct lattice spring model · Gravity increase method

List of symbols

Roman alphabet

A^D	The representative area of a discontinuous spring bond
[C]	The damping matrix
c^D	The cohesion of a discontinuous bond
c^J	The corresponding macroscopic joint parameters
E	The Young's modulus
E_i	The Young's modulus of particle i
E_j	The Young's modulus of particle j
$\sum \mathbf{F}_j^{(t)}$	The total force applied to the particle
f^n	The normal spring force
$\mathbf{F}(t)$	The external force vector
f_t^D	The tensional strength
g_level	The current gravity level
g_max	The maximum gravity level for the simulation
$g(t)$	The gravity increase function
$inter_Loop$	The number of iterations for the sub-calculation
$Loop$	The index of the current iteration
[K]	The stiffness matrix
k_n	The normal spring stiffness
k_n^D	The normal spring stiffness of a discontinuous bond
k_n^J	The macroscopic joint normal stiffness
k_s	The shear spring stiffness
k_s^D	The shear spring stiffness of a discontinuous bond
k_s^J	The macroscopic joint shear stiffness
[M]	The mass matrix
$diag([\mathbf{M}])$	The diagonal elements of the mass matrix

✉ Qin Li
liqintju@163.com

¹ State Key Laboratory of Hydraulic Engineering Simulation and Safety, School of Civil Engineering, Tianjin University, Tianjin 300072, China

² China Railway No. 4 Group Co., Ltd, Hefei 230023, Anhui, China

³ School of Transportation Science and Engineering, Beihang University, Beijing 100191, China

⁴ Department of Geotechnical Engineering, China Institute of Water Resources and Hydropower, Beijing 100048, China

max_Loop	The maximum loop for the simulation
m_p	The mass of a particle
n^{TC}	The total number of spring bonds cut by the same triangle
S^T	The area of the triangle
Δt	The time step
\mathbf{u}	The vector of particle displacement
\mathbf{u}_D^n	The discontinuous spring's normal deformation vector
\mathbf{u}_D^s	The discontinuous spring's shear deformation vector
u^n	The spring's normal deformation
$\mathbf{u}_i^{(t+\Delta t/2)}$	The particle velocity at $t + \Delta t/2$
$\mathbf{u}_i^{(t-\Delta t/2)}$	The particle velocity at $t - \Delta t/2$
$\mathbf{u}_i^{(t+\Delta t)}$	The displacement at $t + \Delta t$
$\mathbf{u}_i^{(t)}$	The displacement at t
u_i^*	The ultimate tensional deformation of the spring
ν	The Poisson's ratio
ν_i	The Poisson's ratio at particle i
ν_j	The Poisson's ratio at particle j
V	The volume of the geometry model

Greek symbols

α^{3D}	The lattice coefficient of a computational model
ϕ^D	The internal friction angle of the discontinuous spring bond
ϕ_i^J	The macroscopic joint friction angle

1 Introduction

Rock slope failure has been observed in a wide range of engineering activities, resulting in the loss of lives and property. Many factors can trigger rock slope failure, such as earthquakes, excessive rainfall, drought, and excavation, as well as tree clearing and deforestation. In general, rock slope stability is controlled by many complex surrounding and internal factors. Most rock slope failures can be categorised into planar failures, wedge failures, toppling failures, and circular failures, of which toppling failures are commonly observed (Adhikary et al. 1997), and some research has been conducted to study their mechanism (e.g. Goodman and Bray 1976; Adhikary and Guo 2002; Alzoubi et al. 2010; Zhang et al. 2010).

An analytical study and an experimental study are two common approaches to practically studying toppling failure of jointed rock slopes. For example, in a classical approach for slope stability analysis, the limit equilibrium (LE) method was extended to study flexural toppling (e.g. Aydan and Kawamoto 1992; Adhikary et al. 1997); however, it was

unable to provide the actual failure surface and mechanism of the flexural toppling. To explore the underlying mechanism of the flexural toppling, small-scale physical tests were conducted using centrifuge tests (e.g. Adhikary et al. 1997; Zhang et al. 2007). The main advantages of these centrifuge tests are that (1) the parameters for the model geometry and mechanical response can be partially controlled and (2) deformation and failure patterns can be easily obtained. However, these requirements are difficult to fully satisfy for natural rock slopes. Meanwhile, centrifuge tests have some shortcomings as well, e.g. the mechanical parameters are difficult and sometimes impossible to precisely control (the friction angle of rock joints cannot reach zero). Furthermore, centrifuge tests are as economically costly and time-consuming as other physical tests.

In recent years, computational methods have been demonstrated as promising approaches to studying rock slope failures (Chen et al. 2015), and they can be generally divided into continuum-based methods and discontinuum-based methods. Finite element methods (FEMs) are the most representative continuum-based methods for analysing slope stability, such as the shear strength reduction method (SSRM) (Zienkiewicz et al. 1975) and the gravity increase method (GIM) (Swan and Seo 1999; Li et al. 2009). The SSRM and GIM are defined as gradually increasing/decreasing the gravity/strength of the computational model until failure, and the factor of safety (FOS) is defined as the ratio of the input gravitational acceleration (or strength) at slope failure to the actual gravitational acceleration (or strength) of the slope. For jointed rock slopes, mechanical behaviours are mostly controlled by rock joints, and the discontinuum-based methods, e.g. the distinct element method (DEM) (Cundall 1971) and discontinuous deformation analysis (DDA) (Shi and Goodman 1985), are suitable candidates. Meanwhile, the SSRM and GIM are applicable as discontinuum-based methods as well. In fact, the GIM can be regarded as a numerical centrifuge test (e.g. Alzoubi et al. 2010). Difficulty in selecting suitable mechanical parameters of the discontinuum-based numerical methods prohibits their full practical application to the analysis of the stability of jointed rock slopes. Generally, the numerical simulation must be calibrated with a physical test. For example, the centrifuge test conducted by Adhikary et al. (1997) has been adopted to calibrate the DEM model of Alzoubi et al. (2010) and verify the FEM model of Adhikary and Guo (2002). However, when setting up the corresponding numerical model, many assumptions must be made, and inconsistencies might occur during this procedure. For example, Adhikary and Guo (2002) used a computational model with the width of 650 mm, whereas Alzoubi et al. (2010) adopted a width of 454 mm. Whether the fixed boundary conditions of these models affect the corresponding results or not is still unclear. In addition, most of the research is mainly focused on parameter study and hardly refers to the toppling failure mechanism of a jointed rock slope

(the different mechanism results between failure *patterns and deformations*).

In this work, flexural toppling failure of a jointed rock slope is further studied using the distinct lattice spring model (DLSM) (Zhao et al. 2011; Zhao 2017). First, the gravity increase method (GIM) is implemented in the DLSM. Next, a computational model using the GIM-DLSM is developed to simulate the centrifuge test conducted by Adhikary et al. (1997) for small-scale model tests of a jointed rock slope. A numerical study on selecting the boundary conditions and material parameters was then conducted, and the results indicate that the GIM-DLSM can reproduce a closer fit to the experimental data on deformation and provide a realistic fracture pattern for the jointed rock slope. The simple failure mechanism adopted by the DLSM provides an alternative explanation for flexural toppling failure of the jointed rock slope. Finally, the influences of the friction angle, cohesion, joint spacing, and joint angle of rock joints on the flexural toppling failure are studied with the GIM-DLSM.

2 The Model

2.1 Gravity Increase Method (GIM)-DLSM

Rock is symbolised as a group of particles with different sizes in the DLSM (Zhao et al. 2011). Similar to the GIM, it is implemented straightforwardly in a FEM (e.g. Li et al. 2009), and a similar procedure can be used for the DLSM. However, some modifications are required for solving this procedure. In this work, when we define the gravity increase function as $g(t)$, the vector of the particle displacement as \mathbf{u} , and the external force vector as $\mathbf{F}(t)$, the equation for the motion of the GIM-DLSM can be expressed as

$$[\mathbf{K}]\mathbf{u} + [\mathbf{C}]\dot{\mathbf{u}} + [\mathbf{M}](\ddot{\mathbf{u}}) = \mathbf{F}(t) + g(t)\text{diag}([\mathbf{M}]) \quad (1)$$

where $[\mathbf{K}]$ represents the stiffness matrix, $[\mathbf{C}]$ the damping matrix, $[\mathbf{M}]$ the diagonal mass matrix, and $\text{diag}([\mathbf{M}])$ the diagonal elements. The dynamic relaxation method is used to solve Eq. (1). Different from the implicit FEM, where the solution can be obtained from a single calculation at a given gravity level, artificial damping must be used for a sub-iteration at a given level of gravity loading. Let us define max_Loop as the maximum loop for the simulation, g_level as the current gravity level, g_max as the maximum gravity level for the simulation, $Loop$ as the index of the current iteration, and inter_Loop as the number of iterations for the sub-calculation. To execute this procedure, we define the current gravity level by using the following equation:

$$g_level = 1 + \frac{g_max - 1}{\left(\frac{\text{max_Loop}}{\text{inter_Loop}}\right)} \text{Mod}(Loop, \text{inter_Loop}) \quad (2)$$

where $\text{Mod}()$ is the remainder operator.

A calculation cycle in the DLSM is performed as follows:

- (a) As particle displacements from the initial position or the previous time step are given, new contacts and broken bonds are formed;
- (b) Contact and spring forces are calculated by using the equivalent constitutive model of spring bonds;
- (c) The individual particle velocity is expressed as

$$\dot{\mathbf{u}}_i^{(t+\Delta t/2)} = \dot{\mathbf{u}}_i^{(t-\Delta t/2)} + \frac{\sum \mathbf{F}_j^{(t)}}{m_p} \Delta t \quad (3)$$

where $\dot{\mathbf{u}}_i^{(t+\Delta t/2)}$ and $\dot{\mathbf{u}}_i^{(t-\Delta t/2)}$ are the particle velocities at $t + \Delta t/2$ and $t - \Delta t/2$, respectively, $\sum \mathbf{F}_j^{(t)}$ is the total force applied to particle j , m_p is the particle mass, and Δt is the time step.

Therefore, a new particle displacement is obtained as

$$\mathbf{u}_i^{(t+\Delta t)} = \mathbf{u}_i^{(t)} + \dot{\mathbf{u}}_i^{(t+\frac{\Delta t}{2})} \Delta t \quad (4)$$

where $\mathbf{u}_i^{(t+\Delta t)}$ and $\mathbf{u}_i^{(t)}$ are the displacements at $t + \Delta t$ and t , respectively. Figure 1 shows the flow chart of the DLSM with the GIM implemented. The procedures in the grey areas are modified for the GIM-DLSM.

2.2 Constitutive Models for Jointed Rock Masses

To model jointed rock masses, two types of spring bonds are required, called the continuous spring bond and discontinuous spring bond. The continuous spring bond is used to represent the rock block, whereas the discontinuous spring bond is adopted for the rock joints. The most distinctive feature of the DLSM is the introduction of a multi-body shear spring to overcome the Poisson's limitation of the classical LSM, and the DLSM evaluates the shear deformation from the local strain rather than the particle displacements. Another distinct feature of the DLSM is that the input parameters are macroscopic material constants. For example, spring parameters k_n and k_s in the DLSM are automatically obtained based on the Young's modulus E and the Poisson's ratio ν using the following equations:

$$k_n = \frac{3}{2\alpha^{3D}} \left(\frac{E_i}{1 - 2\nu_i} + \frac{E_j}{1 - 2\nu_j} \right) \quad (5)$$

$$k_s = \frac{3}{2\alpha^{3D}} \left(\frac{(1 - 4\nu_i)E_i}{(1 + \nu_i)(1 - 2\nu_i)} + \frac{(1 - 4\nu_j)E_j}{(1 + \nu_j)(1 - 2\nu_j)} \right) \quad (6)$$

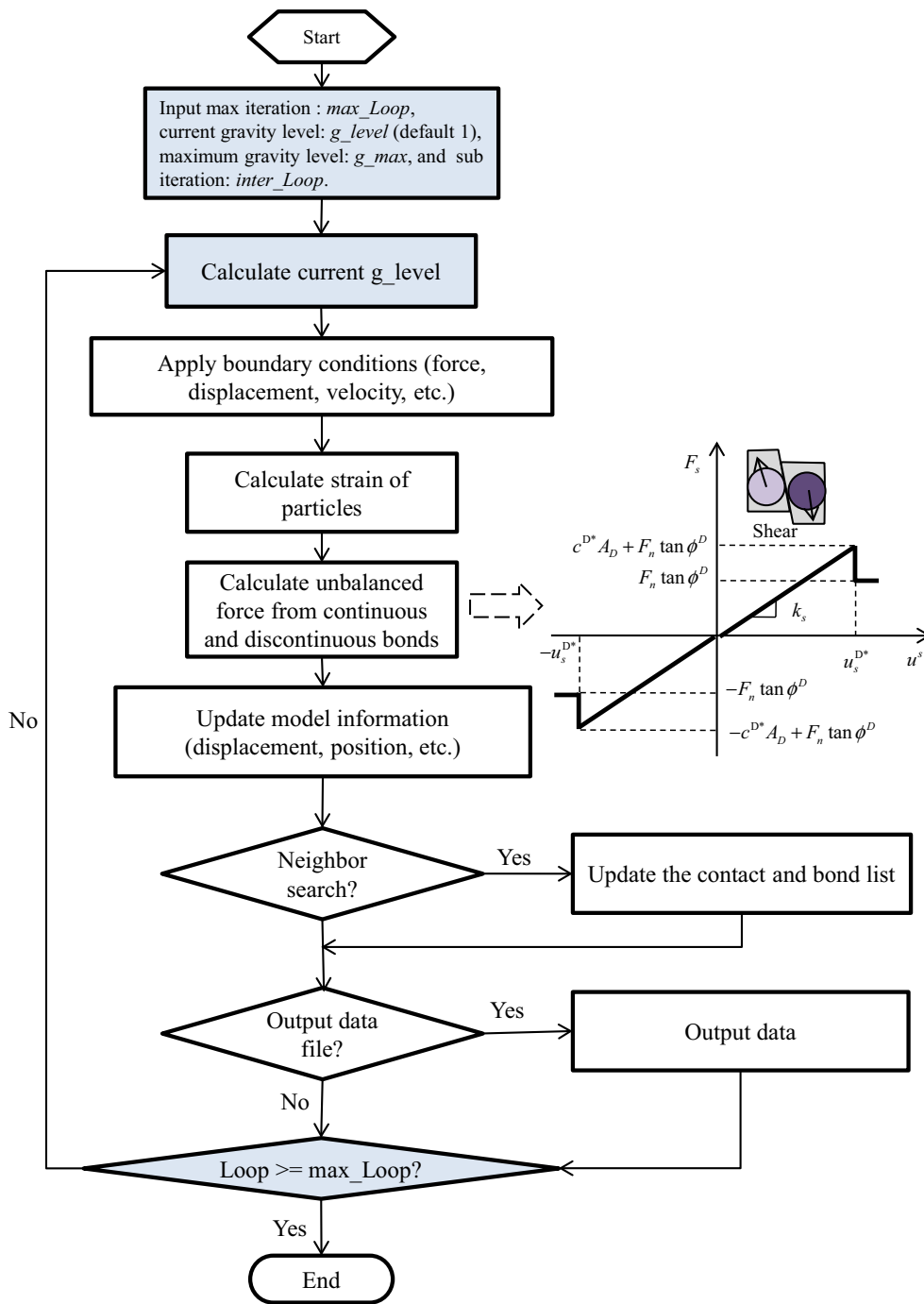


Fig. 1 Flow chart of the DLSSM with the gravity increase method (GIM)

where E_i and E_j are the Young’s moduli of the linked particles, and ν_i and ν_j are the Poisson’s ratios. α^{3D} is a microstructure coefficient of the lattice structure, and it is given as

$$\alpha^{3D} = \frac{\sum l_i^2}{V} \tag{7}$$

where V is the volume of the geometry model and l_i is the length of the i th bond. The constitutive model of the continuous spring bond is represented as

$$f^n = \begin{cases} k_n \cdot u^n, & u^n < u_i^* \\ 0, & \text{else} \end{cases} \tag{8}$$

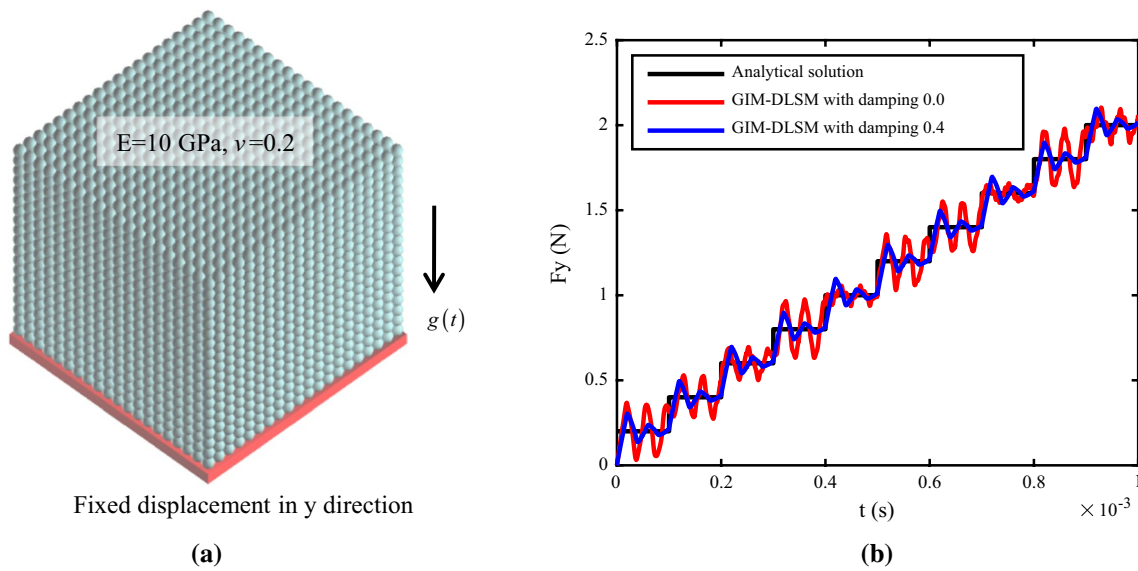


Fig. 2 Influence of the damping coefficient of the GIM-DLSM. **a** Computational model, **b** numerical results and analytical solution

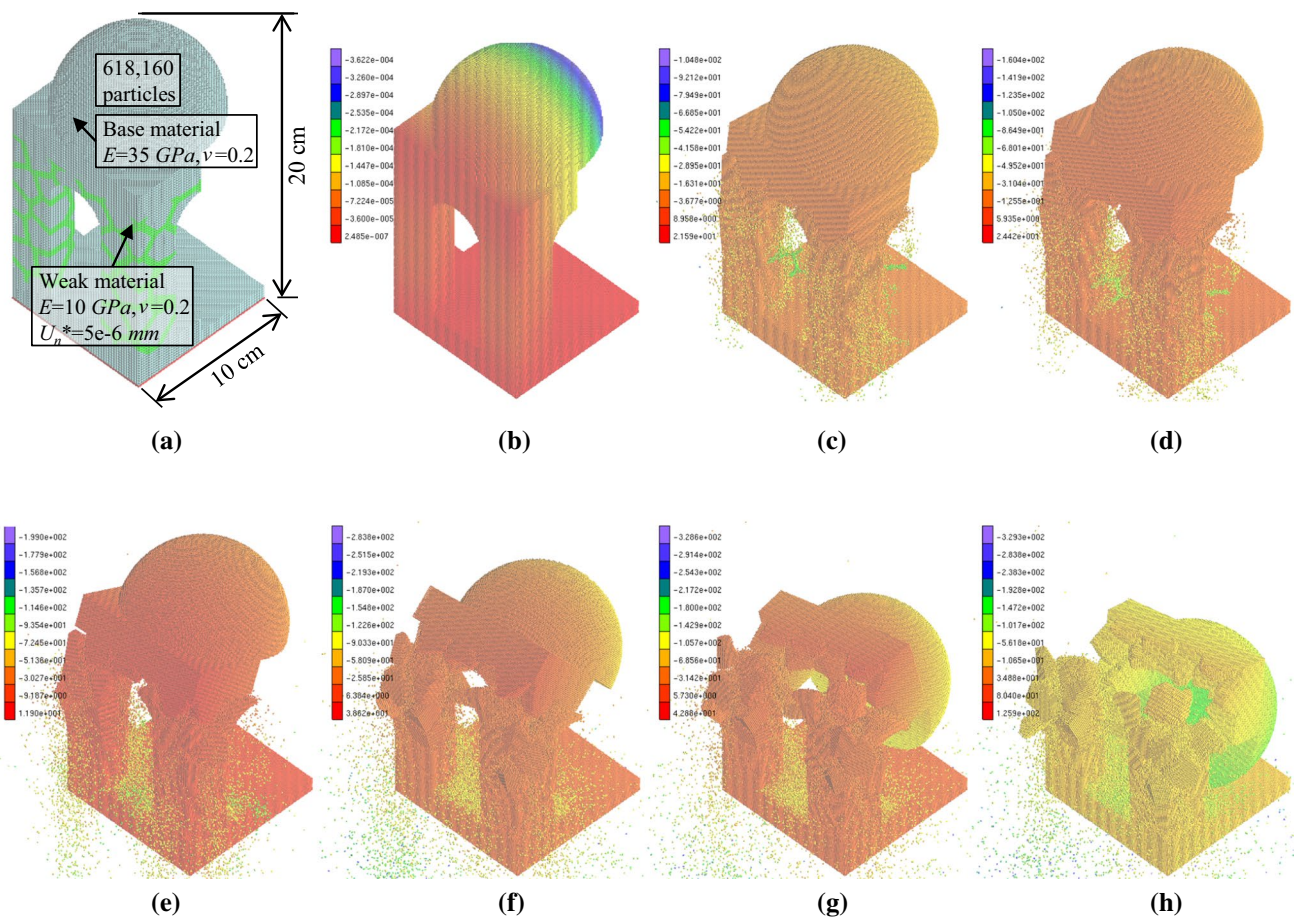


Fig. 3 Modelling a progressive failure problem by using the GIM-DLSM. **a** Computational model, **b** $g_level = 1$, **c** $g_level = 2400$, **d** $g_level = 2700$, **e** $g_level = 3300$, **f** $g_level = 4200$, **g** $g_level = 4800$, **h** $g_level = 6000$

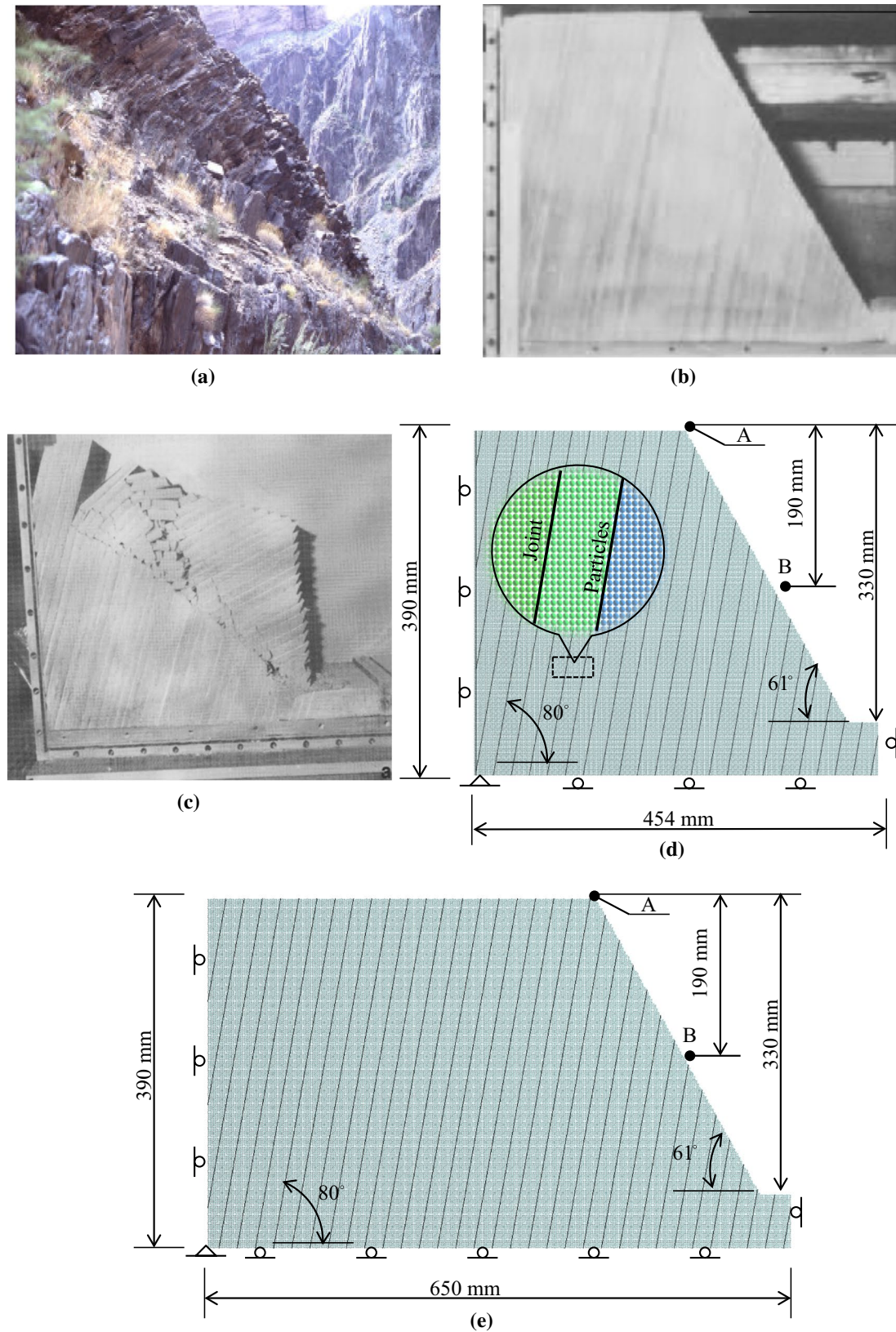


Fig. 4 Flexural toppling failure of a jointed rock slope in the field, the centrifuge test by Adhikary et al. (1997) and the computational models adopted in this work. **a** Flexural toppling failure in the field

(from <http://www.bing.com>), **b** physical model used in the centrifuge test, **c** failure of the jointed rock slope model, **d** computational model I, **e** computational model II

in which f^n is the normal spring force, u^n is the normal deformation, and u_i^* is the ultimate tensional deformation of the spring. A simple brittle model is adopted in this work, and it is capable of simulating the dynamic cracking of poly (methyl methacrylate) (PMMA) (Kazerani et al. 2010), the dynamic fracturing of coal (Zhao et al. 2014b), and the tensile failure of sandstone (Zhao et al. 2014a). This constitutive model provides a simple and fundamental assumption for the mesoscopic failure of the simulated rock block. The advantage of using the DLSSM is its ability to set up a complex macroscopic failure phenomenon from simple microscopic events.

To model the jointed rock, discontinuous spring bonds were required (Zhao 2015). They were developed from continuous spring bonds cut by triangles (geometrically represented joints). The Mohr–Coulomb model was adopted for the discontinuous spring bonds, and the force and displacement relationships are given as (Zhao 2015)

$$\mathbf{F}^n = \begin{cases} k_n^D \cdot \mathbf{u}_D^n, & k_n^D(\mathbf{u}^n \cdot \mathbf{n}) < \sigma_i^J A^D \\ 0, & \text{else} \end{cases} \quad (9)$$

$$\mathbf{F}^s = \begin{cases} k_s^D \cdot \mathbf{u}_D^s, & k_s^D \|\mathbf{u}_D^s\| < c^J A^D + (\mathbf{F}_n \cdot \mathbf{n}) \cdot \tan \phi^J \\ (\mathbf{F}_n \cdot \mathbf{n}) \cdot \tan \phi^J \mathbf{u}_D^s / \|\mathbf{u}_D^s\|, & \text{else} \end{cases} \quad (10)$$

where k_s^D and k_n^D are normal and shear spring stiffness, respectively, and \mathbf{u}_D^n and \mathbf{u}_D^s are spring deformations. The

mechanical parameters of bonds are calculated using the following equations:

$$k_n^D = k_n^J A^D \quad (11)$$

$$k_s^D = k_s^J A^D \quad (12)$$

$$f_i^D = \sigma_i^J A^D \quad (13)$$

$$c^D = c^J A^D \quad (14)$$

$$\phi^D = \phi^J \quad (15)$$

where k_n^D is the normal spring stiffness, k_s^D is the shear spring stiffness, f_i^D is the tensional strength, c^D is the cohesion, ϕ^D is the internal friction angle of the discontinuous spring bond, and $k_n^J, k_s^J, c^J,$ and ϕ^J are the corresponding macroscopic joint parameters. Moreover, A^D represents the area of a discontinuous spring bond and can be determined as follows

$$A^D = \frac{S^T}{n^{TC}} \quad (16)$$

where S^T is the area of the triangle and n^{TC} is the total number of spring bonds cut by the same triangle.

2.3 Long-time Simulation for the Centrifuge Test

Although $g(t)$ can be directly input as the boundary condition in an implicit scheme, in an explicit scheme such as the DLSSM, the time step used in an explicit solution is usually very small, and running a full-time simulation for a

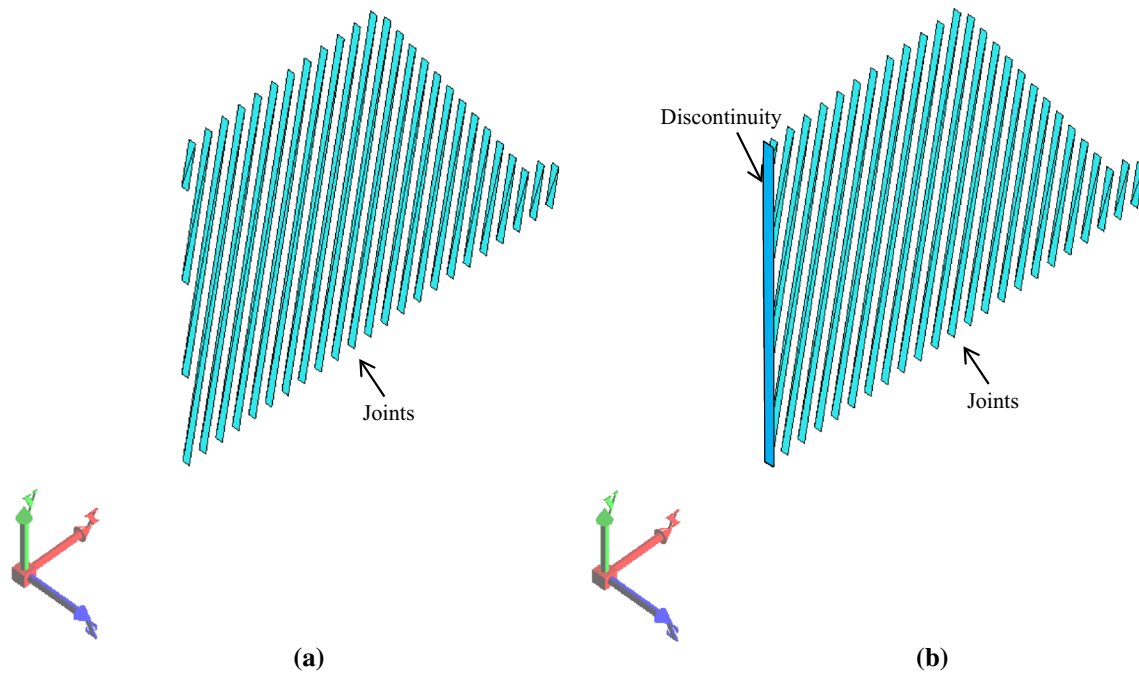


Fig. 5 Two joint settings for representing different boundary conditions of the physical test. **a** Joint setting case A, **b** joint setting case B

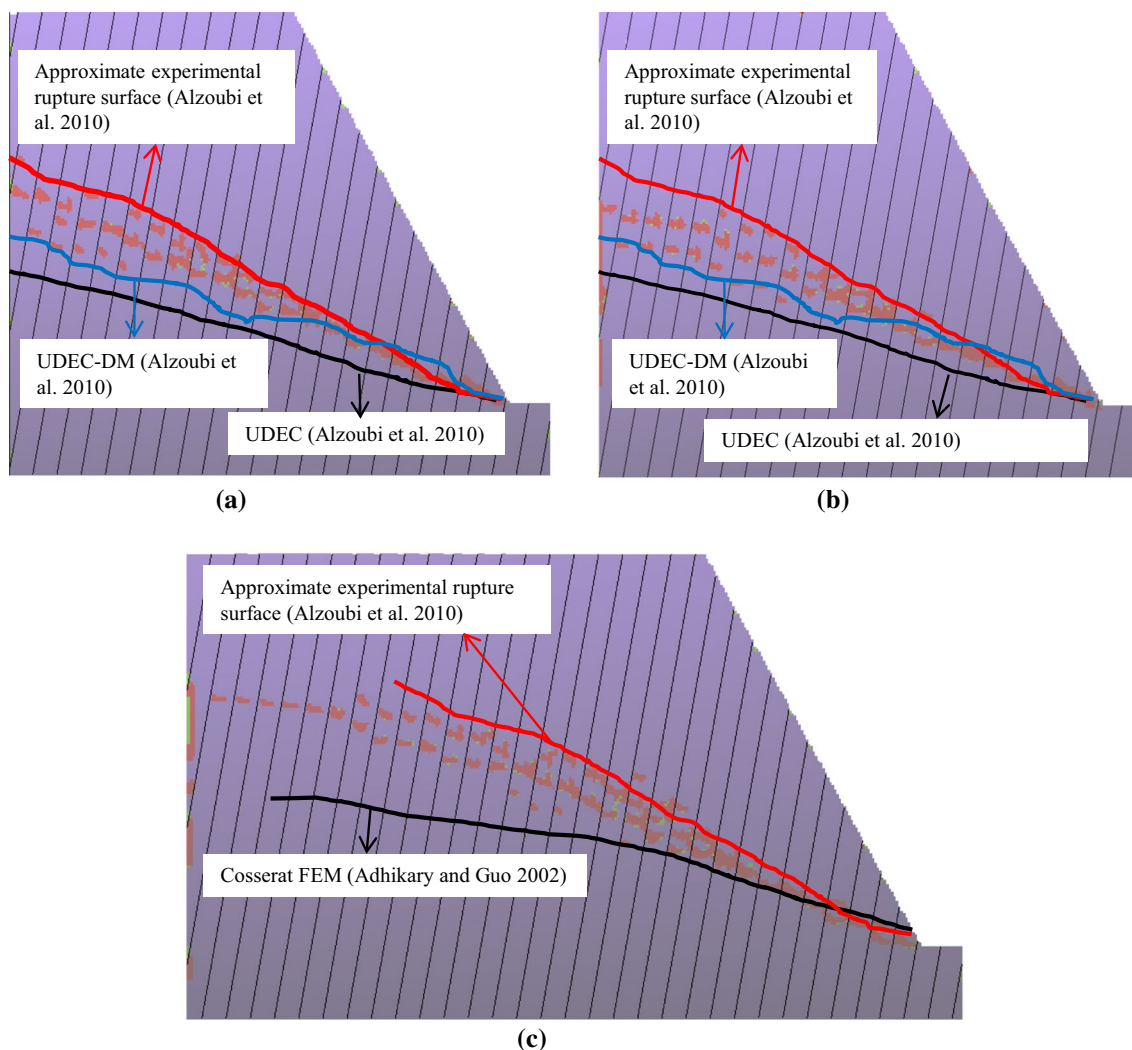


Fig. 6 Comparison among the failure patterns predicted by the GIM-DLSM with different boundary conditions (model I refers to the computational model shown in Fig. 4d; model III refers to the com-

putational model of Fig. 4d with the boundary conditions shown in Fig. 5b; model II refers to the computational model shown in Fig. 4e). **a** Model I, **b** Model III, **c** Model II

centrifuge test is computationally time prohibitive. To solve this contradiction, a different time line in the numerical simulation from that in the centrifuge test is considered. In the GIM-DLSM, when the mechanical damping is applied, the final solution is regarded as a quasi-static solution, and the time step loses its physical meaning. To utilise this feature of the DLSM for a long-time simulation, the time line is replaced by a gravity curve with a staircase at the beginning. Then, for each stair, a quasi-static calculation is adopted to obtain the equilibrium state of the model under a given level of gravity. Finally, the numerical centrifuge test can be transferred into a sequence of loadings under given gravity points (taken from the recorded gravity history in the centrifuge test).

To examine the idea above, a cube is loaded with a given gravity function (see Fig. 2), and the reaction force applied

to the bottom is recorded during the simulation process. The results predicted by the GIM-DLSM are illustrated in Fig. 2. It can be seen that the prediction of the GIM-DLSM reasonably fits the corresponding analytical solution, and the damping affects the vibration of the solution. Here the local damping (adopted in the DEM by Dr. Cundall as well) is used. It is a dimensionless coefficient and represents the ability of the kinematic energy absorption. When the damping is 0.4, equilibrium can be achieved in each sub-step. However, the vibration does not propagate (become larger) during calculation, which indicates that the error caused by time scaling (number of steps used in each sub-step) can be localised. Therefore, a long-time simulation can be well handled by using the DLSM with a staircase gravity curve.

Although the implementation of the GIM-DLSM is straightforward, the effect is very impressive. Figure 3 shows

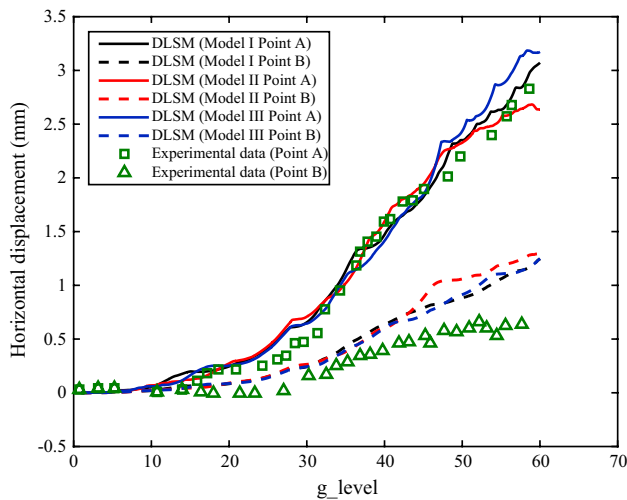


Fig. 7 Displacements of two measuring points predicted by the GIM-DLSM and experimental tests

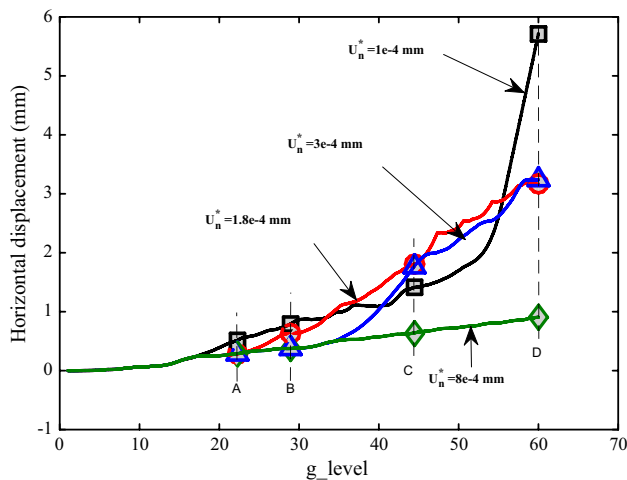


Fig. 8 Influence of the tensional strength of the rock block on the deformation of the jointed rock slope

a numerical centrifuge test of a model composed of more than a half million particles. To obtain an intensive collapse, the maximum gravity level is set as 6000 g. As g_level is increased to 2700, only slight damage and deformation are observed in Fig. 3b–d, whereas extremely large damage and deformation are indicated in Fig. 3e–h. This phenomenon occurs due to the travelling distance of a free particle being longer with higher g_level , which results in a longer simulated time under higher gravity. In this work, we will adopt the GIM-DLSM for the stability analysis of toppling failure of jointed rock slopes. It should be mentioned that the jointed DLSM (Zhao 2015) still cannot solve the large deformation problems, due to the reason that the constitutive model of joints (Eqs. 9 and 10) did not include the influence

of the large rigid body rotation. Therefore, our simulations only focus on fractures of the jointed rock slope under small deformations.

3 Calibration

Flexural toppling failure of jointed rock slopes commonly occurs in the field (see Fig. 4a), where large deformation and an apparent failure surface can occur even though the slope is stable. Fracture and deformation of a slope would make people scared to fully utilise its surrounding infrastructure, i.e. the flexural toppling of a reservoir slope in a hydraulic power station could result in not fully filling the reservoir and generating electricity normally.

To study flexural toppling failure of jointed rock slopes, seven small-scale model tests of jointed rock slopes were conducted using the geotechnical centrifuge of the University of Western Australia (Adhikary et al. 1997). With the purpose of confirming data completeness, one centrifuge test, originally simulated using the FEM (Adhikary and Guo 2002) and the DEM (Alzoubi et al. 2010), is further utilised for calibration of the GIM-DLSM.

Figure 4 shows the physical model and corresponding computational models, and their parameters are as follows: slope height 330 mm, slope dip angle 61° , joint spacing 10 mm, joint dip angle 80° , and particle radius 1 mm. Two computational models with different widths are used to examine the difference between the geometrical models used by Adhikary and Guo (2002) and Alzoubi et al. (2010). Figure 4b, d represents the model configuration and the failure pattern of Alzoubi et al. (2010) (114,600 particles), and Fig. 4e refers to the computational model of Adhikary and Guo (2002) (212,100 particles). When conducting the numerical test, we used a wider model of Adhikary and Guo (2002) to eliminate the influence of the fixed boundary conditions applied for the left boundary.

As shown in Fig. 5, to further explore the influence of the left boundary condition, two different settings were adopted for the model in Fig. 4d. The main difference is that a vertical discontinuity with a tensional strength of zero was used for the model, and it reproduced a boundary condition that could barely withstand compression loading from the model to mimic the model’s framework effect (see Fig. 4b). The material parameters for the block in the research of Adhikary et al. (1997) were recorded as follows: elastic modulus 2.2–2.6 GPa, Poisson’s ratio 0.16, and density 2380 kg/m^3 . These parameters are directly used in our modelling (the elastic modulus adopted is 2.4 GPa). For the joints, there are five parameters, the normal stiffness, the shear stiffness, the friction, the cohesion, and the tensile strength, of which the friction is given (reported from 22° to 26°), and the rest of the parameters need to be calibrated via a comparison

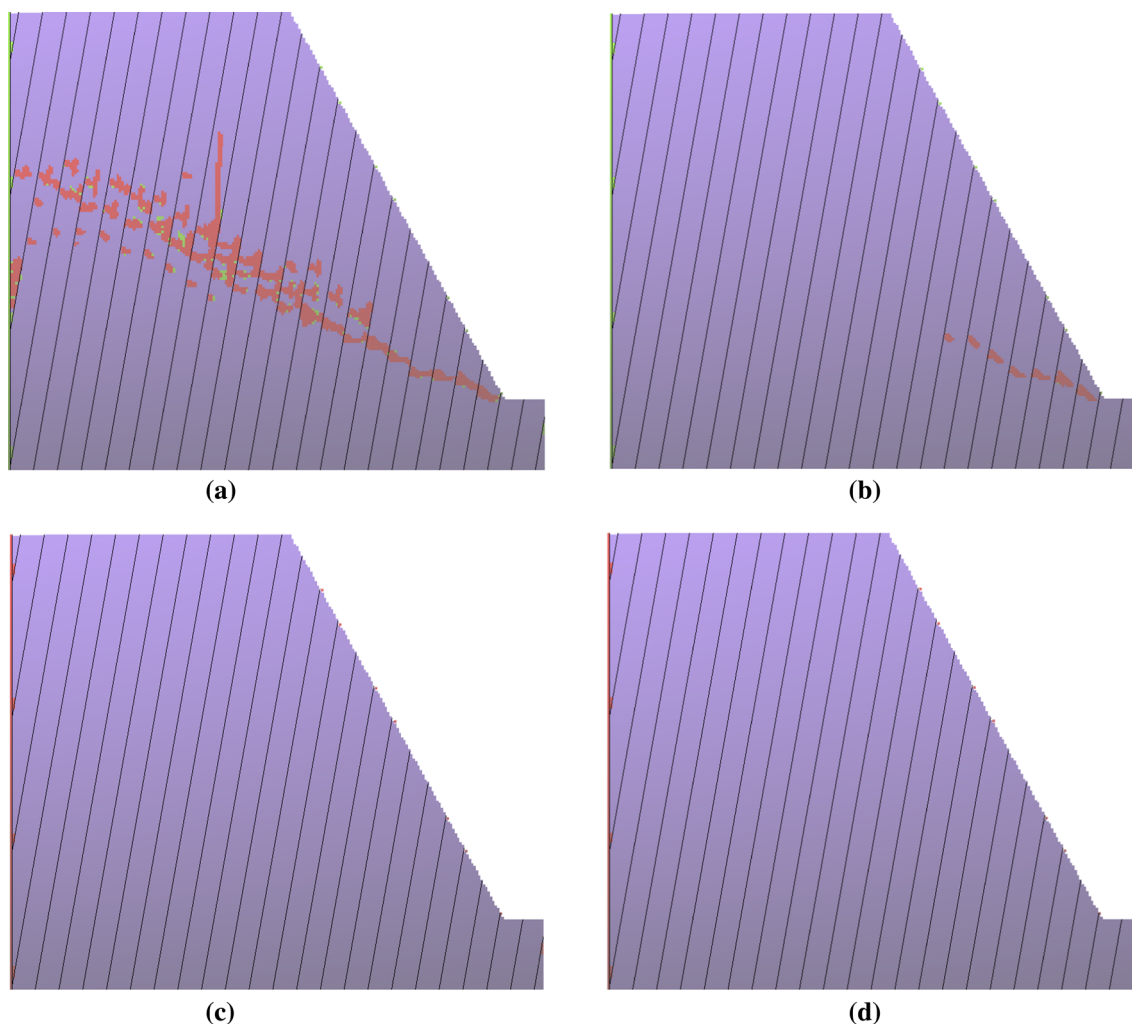


Fig. 9 Failure patterns of the jointed rock slope under g_level Point A (the unit of U_n^* is mm, red refers to the failure particles with opening, and green refers to failure with closure). **a** $U_n^* = 1e-4$, **b** $U_n^* = 1.8e-4$, **c** $U_n^* = 3e-4$, **d** $U_n^* = 8e-4$

between the displacements predicted by the numerical simulation and the corresponding experimental results of the centrifuge test. Since the Universal Distinct Element Code (UDEC) modelling (Alzoubi et al. 2010) was conducted to calibrate these joint parameters, the DLSM could use the macroscopic joint parameters directly. In this work, the same parameters can be adopted, and the only adjustable parameter is the tensile strength of the rock block. Since the calibration process is complex and time-consuming, a parallel DLSM solver (Zhao et al. 2013) is adopted. To reproduce experimental displacements, all the parameters used in the GIM-DLSM are as follows: the normal stiffness and shear stiffness of joints 400 GPa/m, the friction angle 24 degrees, the tensile strength of the joints 0 kPa, the cohesion of the joints 5 kPa, the tensile limit of the normal spring for the rock block $5e-4$ mm, the time step $1.5e-6$ s, and the local damping coefficient 0.40. The cubic-II lattice structure is adopted for all the simulations in this work, which means

that the average number of the lattice per particle is about 18.

Figure 6 shows the failure patterns of these models using the same set of calibrated parameters. The results show that the GIM-DLSM reproduces the closest fitting with the experimental results, and these three computational models reproduce similar failure patterns. To realise a comparison in quantity, the displacements at two measuring points of these models and the experimental tests are plotted together in Fig. 7. It should be mentioned that although small differences were observed between these computational models in Fig. 4, significant differences might be caused by changing the configurations of the model, e.g. changing the joint angle to 0. Computational model III is the closest to the actual physical test, and it is adopted as the model configuration in the other parts of this work.

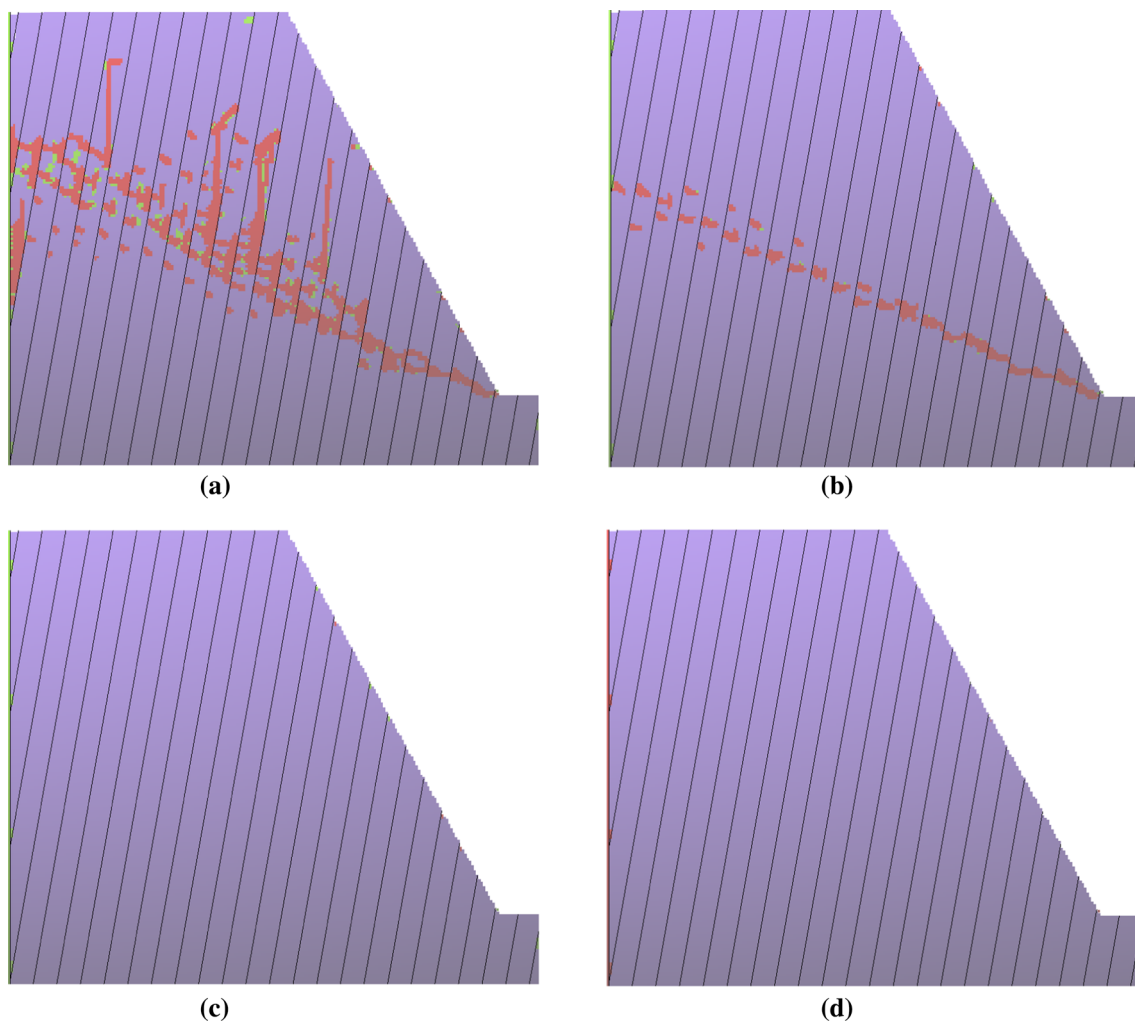


Fig. 10 Failure patterns of the jointed rock slope under g_level Point B (the unit of U_n^* is mm). **a** $U_n^* = 1e-4$, **b** $U_n^* = 1.8e-4$, **c** $U_n^* = 3e-4$, **d** $U_n^* = 8e-4$

4 Discussion

In this section, the influences of mechanical and geometrical parameters on the failure patterns and deformations of flexural toppling failure of a jointed rock slope are investigated using the GIM-DLSM.

4.1 Tensional Strength of the Rock Block

Figure 8 shows the simulation results for measuring point A, which are based on different tensional strengths of the rock block. It reveals the mechanism of the deformation and fracturing of the jointed rock slope caused by microscopic failure of the rock block. When g_level is low (see Fig. 8), two groups are derived from deformation. The first group is the model with the tensional strength of $1e-4$ mm, and the other group is the one with higher tensile strengths. When looking at the failure patterns of these models (see Fig. 9),

we can find that the first group produces an apparent failure surface, which indicates that the deformation of the flexural toppling failure mainly arises from the microscopic tensile failure of the rock block. As g_level increases to level B (see Fig. 8), the second model (with the tensile strength of $1.8e-4$ mm) moves upward to the first group, which can be reflected in the failure patterns of these models (see Fig. 10) as well.

Comparing the damage degree with the induced deformation, multiple fractures do not seem to influence the deformation, and a nonlinear relationship exists between the fracture degree and the induced deformation. This conclusion is further confirmed by the deformation and failure pattern shown at the g_level of C in Fig. 11, where the model with the tensile strength of $3e-4$ mm moves to the first group. When the slope is severely damaged, a large jump might occur in the model with the tensile strength of $1.8e-4$ mm at the g_level of D, as shown in Fig. 12.

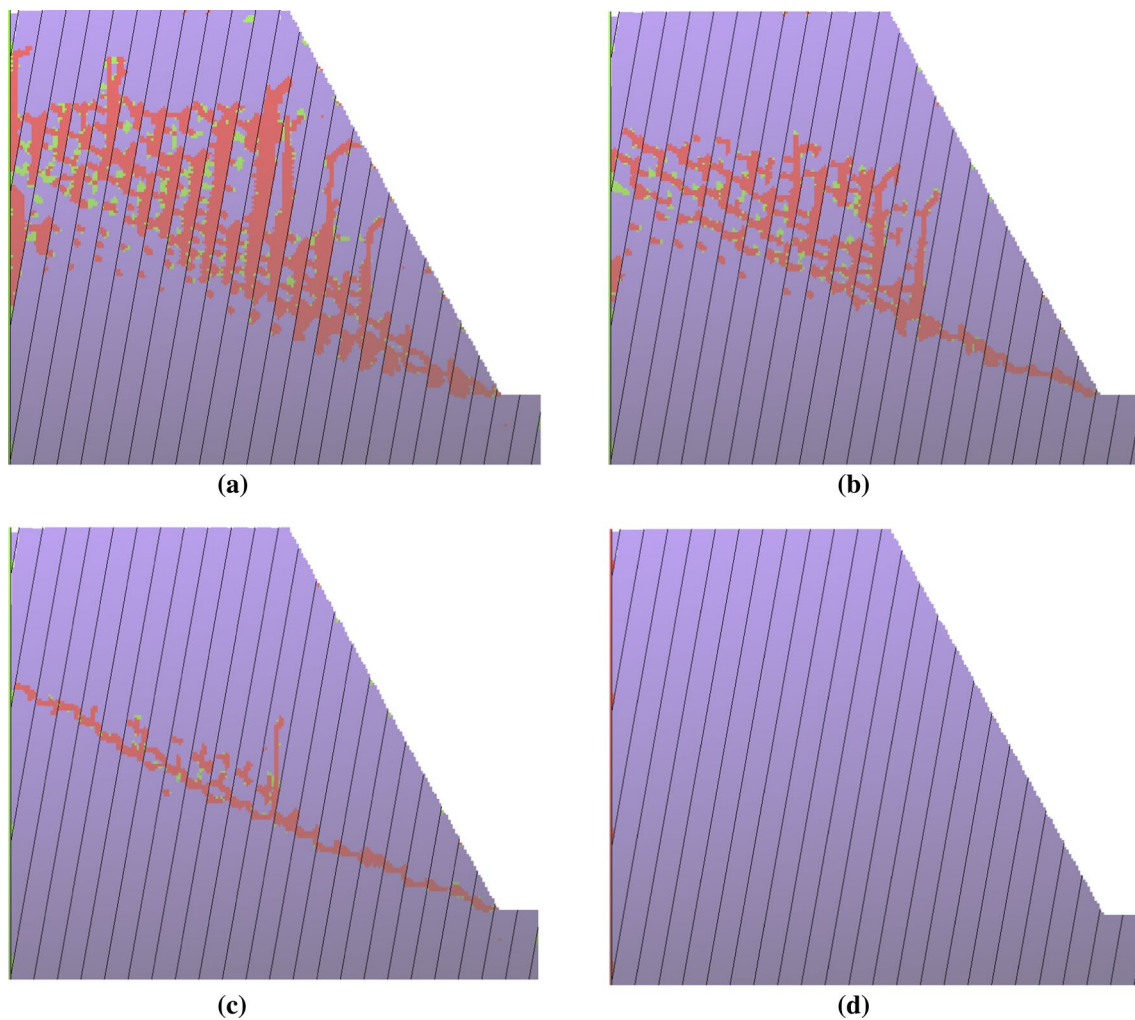


Fig. 11 Failure patterns of the jointed rock slope under g_level Point C (the unit of U_n^* is mm). **a** $U_n^* = 1e-4$, **b** $U_n^* = 1.8e-4$, **c** $U_n^* = 3e-4$, **d** $U_n^* = 8e-4$

Therefore, it could be concluded that the deformation of a jointed rock slope is controlled by both g_level and the fracture surface. However, the failure pattern of a slope is not influenced by the tensional strength of the rock block, which indicates that the deformation history of measuring points, rather than the fracture pattern, is a suitable candidate for calibrating the tensional strength of the jointed rock slope.

4.2 Joint Cohesion

The joint cohesion is set to 0, 10, and 15 kPa (other parameters for the model are the same as in the above section), and the simulation results of displacements at measuring points are shown in Fig. 13. When cohesion increases, the deformation will decrease, and when g_level is greater than 40, the result at measuring point A shows a greater fluctuation than that at measuring point B. In fact, measuring point A is at the top of the slope. As the toppling occurs, a greater

disturbance is expected (due to the principle of leverage, see Fig. 4). This implies that the measured displacement at the post-failure stage could be used for calibrating the joint cohesion. To further explore the mechanism, the failure surfaces of these models are plotted in Fig. 14. It can be seen that the failure angle of the jointed rock slope enlarges as the cohesion increases, but the variations are small. Therefore, the rupture pattern of the toppling failure cannot be used to calibrate the joint cohesion. In addition, it is concluded that the flexural toppling of a jointed rock slope is only slightly influenced by the joint cohesion.

4.3 Joint Friction Angle

Figure 15 shows the displacements of the model with different friction angles, and the joint friction angles significantly influence displacements at two measuring points. In general, the results of the joint friction angle are quite different from

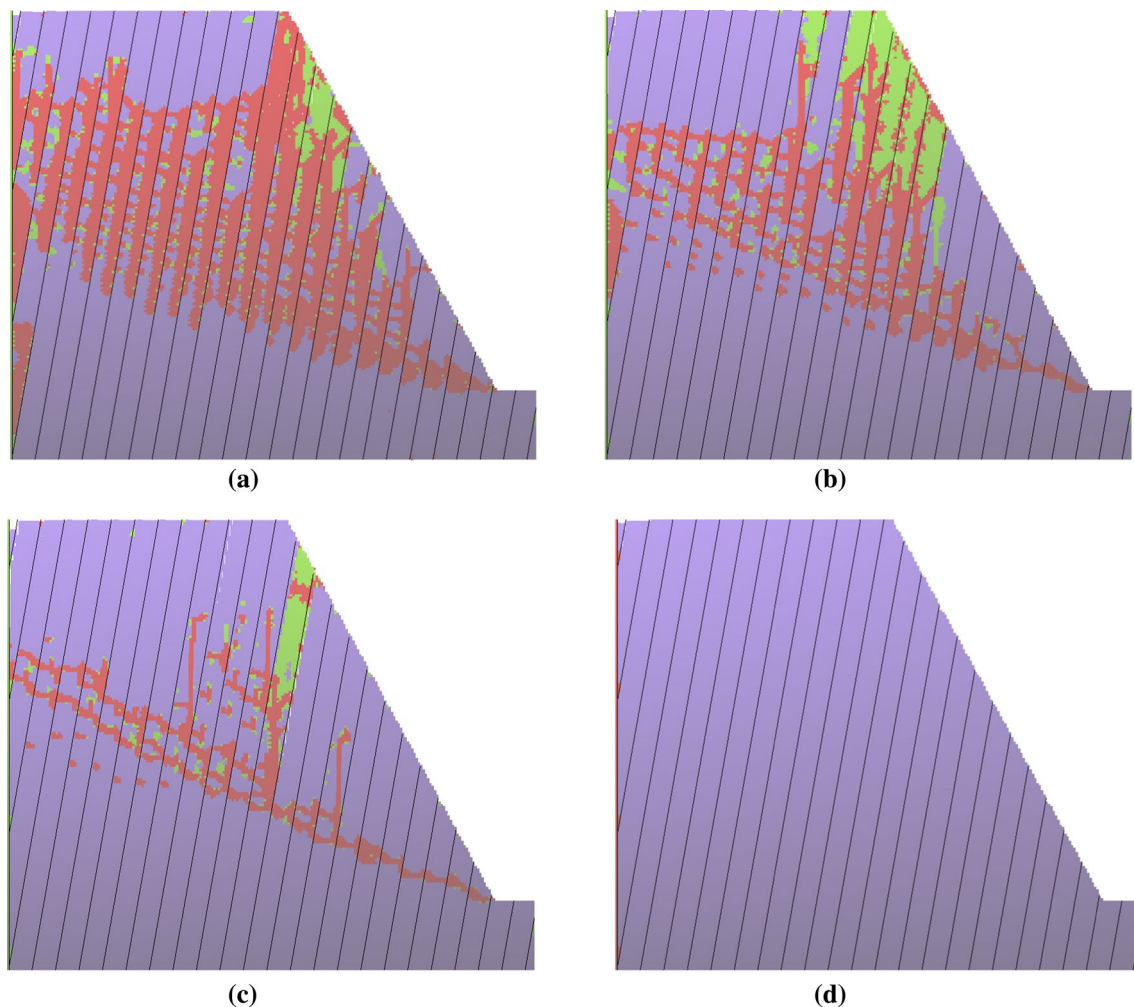


Fig. 12 Failure patterns of the jointed rock slope under g_level Point D (the unit of U_n^* is mm). **a** $U_n^* = 1e-4$, **b** $U_n^* = 1.8e-4$, **c** $U_n^* = 3e-4$, **d** $U_n^* = 8e-4$

those of the cohesion. When the joint angle is large (40°), the deformation of the measuring points is quite small. In addition, the difference between measuring points A and B is nearly negligible, which indicates that the displacement of these two points mainly arise from the deformation of the rock block rather than the slip of joints. As the joint friction angle is reduced to 10° , the displacement of these two measuring points increases, and the difference between these two measuring points enlarges. However, when the friction angle continues to decrease to 0° , there is no change in the difference between the displacement of measuring points A and B. This implies that there is an upper limit for the influence of the joint friction on the deformation of the jointed rock slope.

Figure 16 shows the failure patterns of a jointed rock slope with different joint friction angles for further exploration. It can be seen that the failure surface angle increases and the displacement decreases as the friction angle

increases. When looking locally at the cracks in the rock block, we discover that these cracks tend to be perpendicular to the joint surface, whereas the direction of the macroscopic fracture surface formed by these tiny cracks is not perpendicular to the joint surface and is significantly influenced by the joint friction angle.

4.4 Joint Spacing

Models with different joint spacings are further calculated by using the GIM-DLSM, and the displacements at the measuring points are shown in Fig. 17. It can be seen that an overall decrease in the displacement of the jointed slope could be obtained by increasing the joint spacing, and the effect of joint spacing at point B is greater than that at point A. The reason for this result may be that the displacement at point A is mainly caused by the rotation of the failure zone. The main decisive factor is the distance

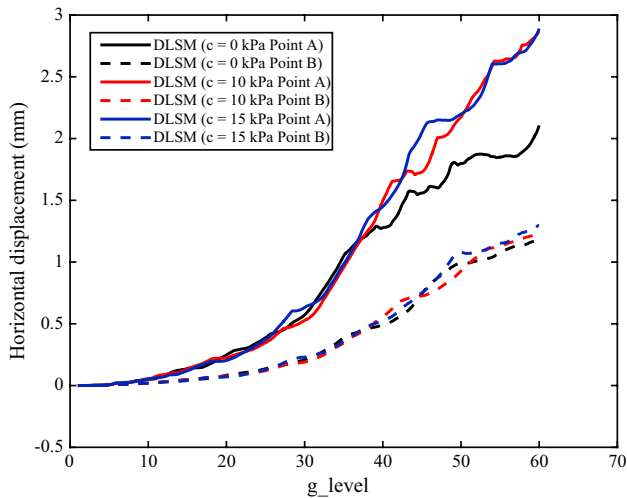


Fig. 13 Deformation at two measuring points under different joint cohesions

from the rupture surface, and different joint spacings do not cause significant diversity in terms of rigid body rotation of the failure zone. However, the displacement at point B is more affected by the translation, and this translation is caused by the deformation of the damaged zone, which is more affected by the joint spacing. This explanation is further confirmed by the failure patterns in Fig. 18. The failure surfaces of these models are only slightly different, and the fracture angle and failure location are close to each other. The difference between rupture patterns caused by the joint spacing is the local failure around the foot area. Specifically, when the joints are very dense or very sparse, the fracture surfaces have certain curvatures; however, the curvatures of the fracture surfaces are more or less straight at the joint spacing of 30 m. It is implied that the jointed rock slope fracturing behaviours are close to that of the continuum medium when there are too many or only a few joints.

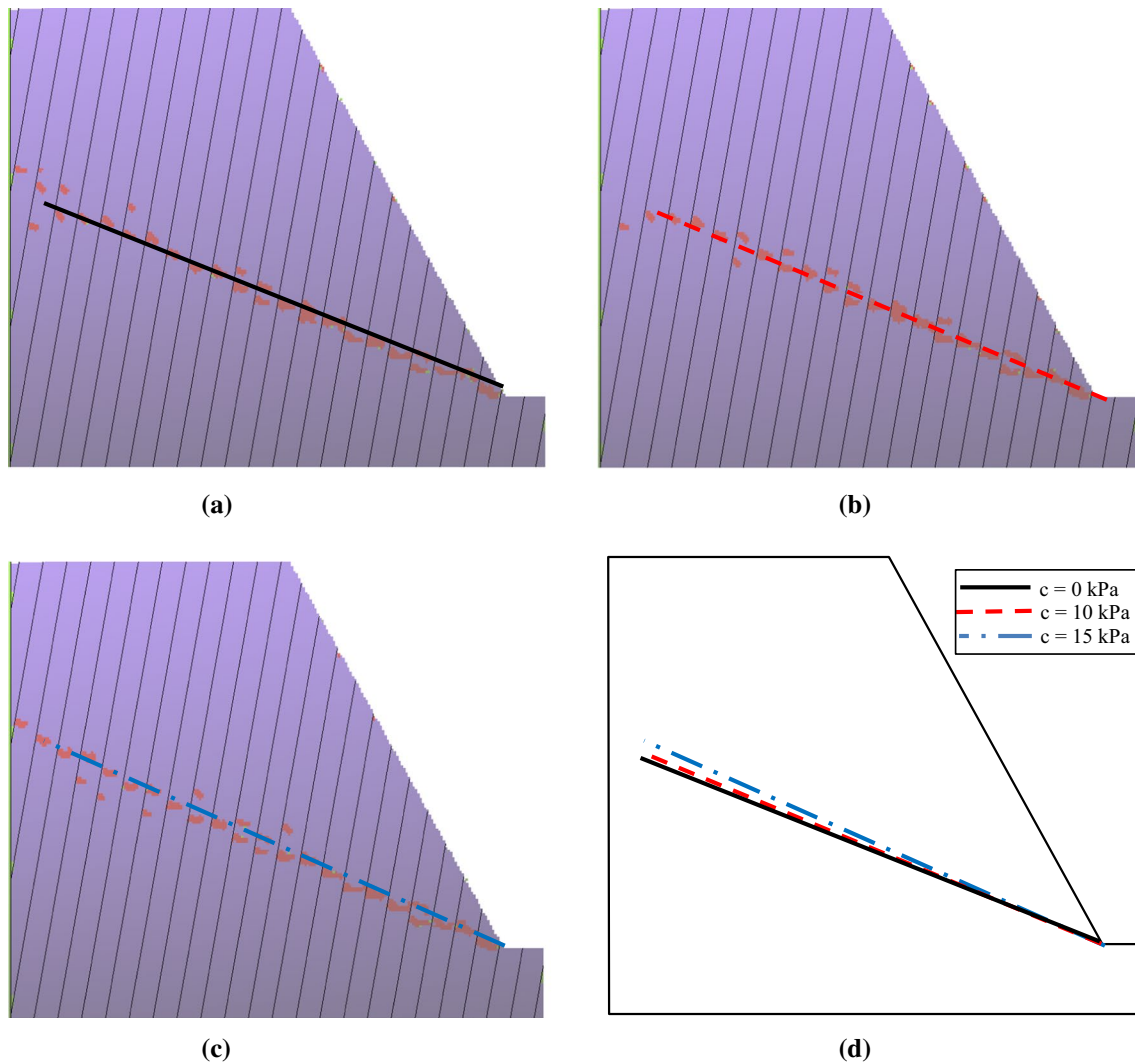


Fig. 14 Fracture surface of the jointed rock slope under different joint cohesions. **a** $c = 0$ kPa, **b** $c = 10$ kPa, **c** $c = 15$ kPa, **d** comparison

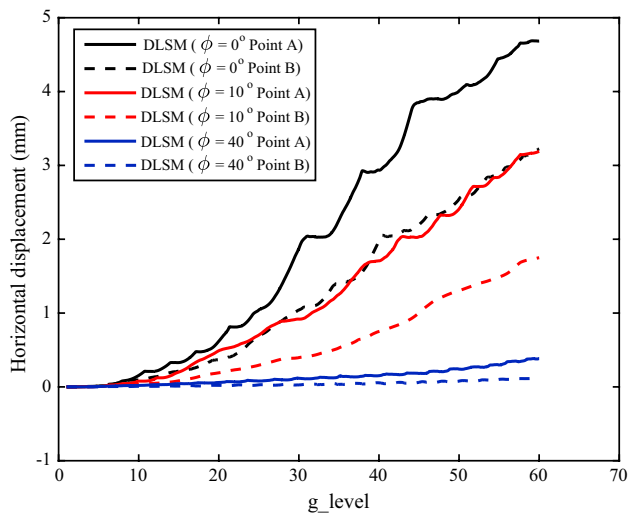


Fig. 15 Deformation at two measuring points under different joint internal friction angles

4.5 Joint Angle

The measured displacement of the joint angle has a feature of first increasing and then decreasing (Fig. 19), and the deformation is largest when the joint angle is 70° . Figure 20 shows the fracture surfaces of the rock slope with different joint angles. The rupture angles, as well as the angle between the fracture surface and the horizontal line, are approximately 5° , 20° and 50° when the joint angles are 85° , 70° and 40° , which indicates that the rupture direction is perpendicular to the joint. The results indicate that the joint angle is also a decisive factor for the toppling failure of the rock slope.

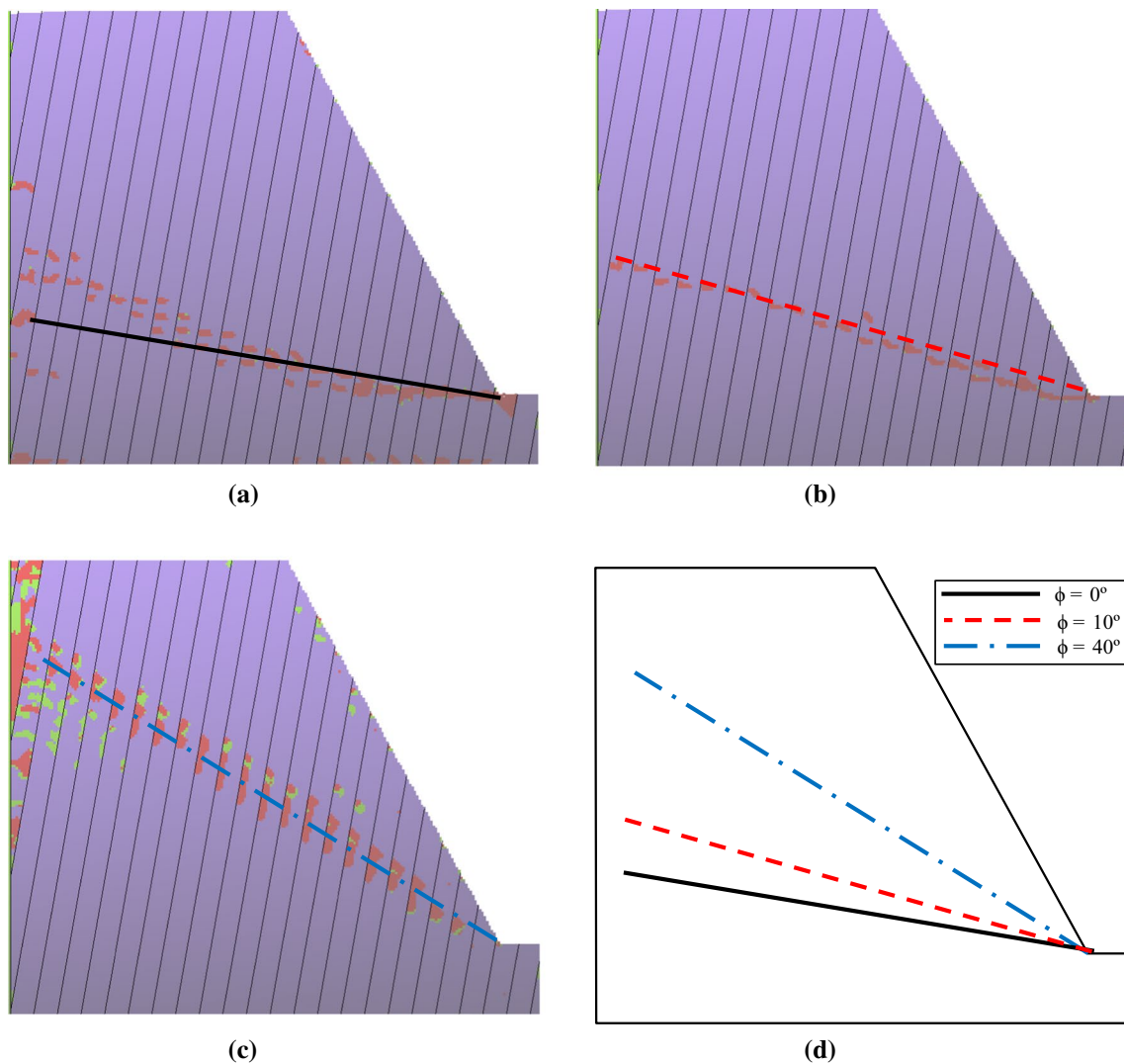


Fig. 16 Fracture surface of the jointed rock slope under different joint internal friction angles. **a** $\phi = 0^\circ$, **b** $\phi = 10^\circ$, **c** $\phi = 40^\circ$, **d** comparison

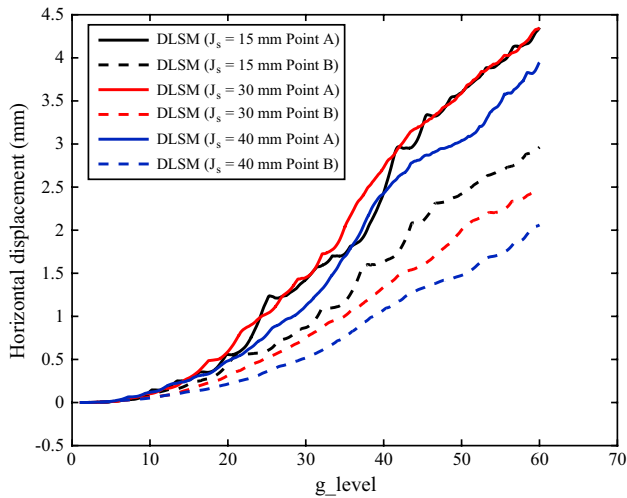


Fig. 17 Deformation at two measuring points under different joint spacings

5 Conclusions

The GIM-DLSM has been successfully implemented for the analysis of flexural toppling failure of jointed rock slopes. Both displacements and fracture patterns were reasonably captured using the GIM-DLSM with a set of calibrated parameters and boundary conditions. In addition, an analysis of parameters was conducted to study the influences of the cohesion, the strength of the rock block, the friction angle, the joint spacing and the joint angle on the flexural toppling failure of the jointed rock slope.

Based on the numerical simulation of the GIM-DLSM, it is concluded that the flexural toppling failure of the jointed slope is slightly influenced by joint cohesion and joint spacing, whereas both failure patterns and deformation are significantly influenced by the friction angle and the joint angle. The toppling rupture pattern of the jointed rock slope is not mainly controlled by the strength of the rock block, whereas

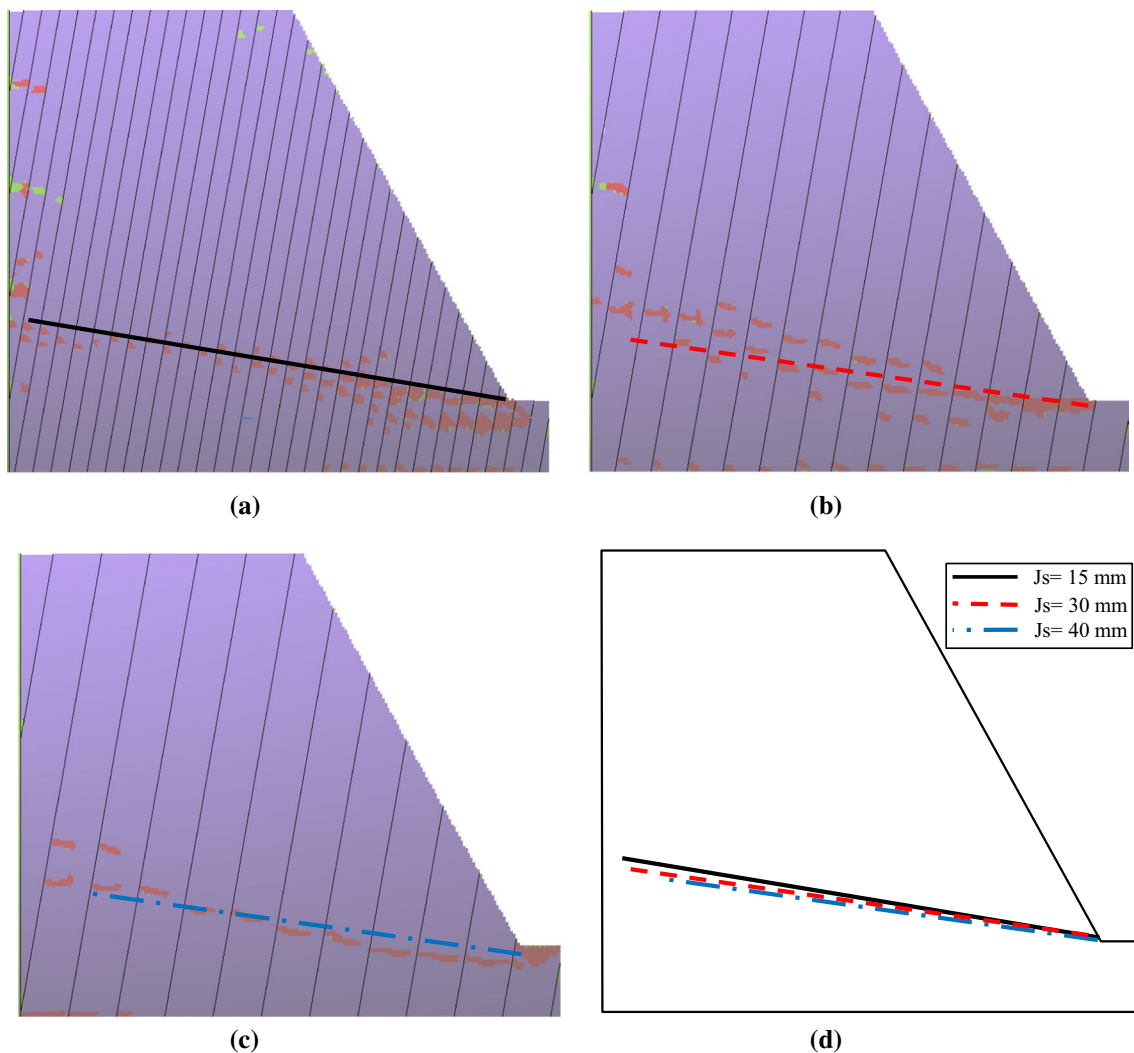


Fig. 18 Fracture surface of the jointed rock slope under different joint spacings. **a** $J_s = 15$ mm, **b** $J_s = 30$ mm, **c** $J_s = 40$ mm, **d** comparison

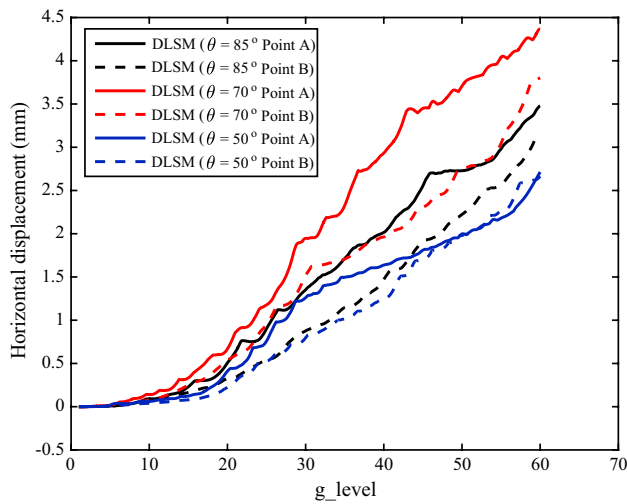


Fig. 19 Deformation at two measuring points under different joint angles

the block strength influences the deformation of the jointed rock slope.

Therefore, to evaluate the safety situations of jointed rock slopes in terms of flexural toppling failure in practice, obtaining reasonable block strengths, friction angles of the joints and joint angles is essential. Moreover, this conclusion can also be used in a reverse way, meaning that the joint friction can be back-calculated from the actual slope failure pattern when the geometry information of the joint is given. After that, the strength of the rock block can be further calibrated using the deformation records of the jointed rock slope. Based on our simulation results, it can be concluded that the most efficient way to prevent flexural toppling failure (too large deformation) is to enrich the friction angle of the joint, e.g. by grouting concrete into the rock joints.

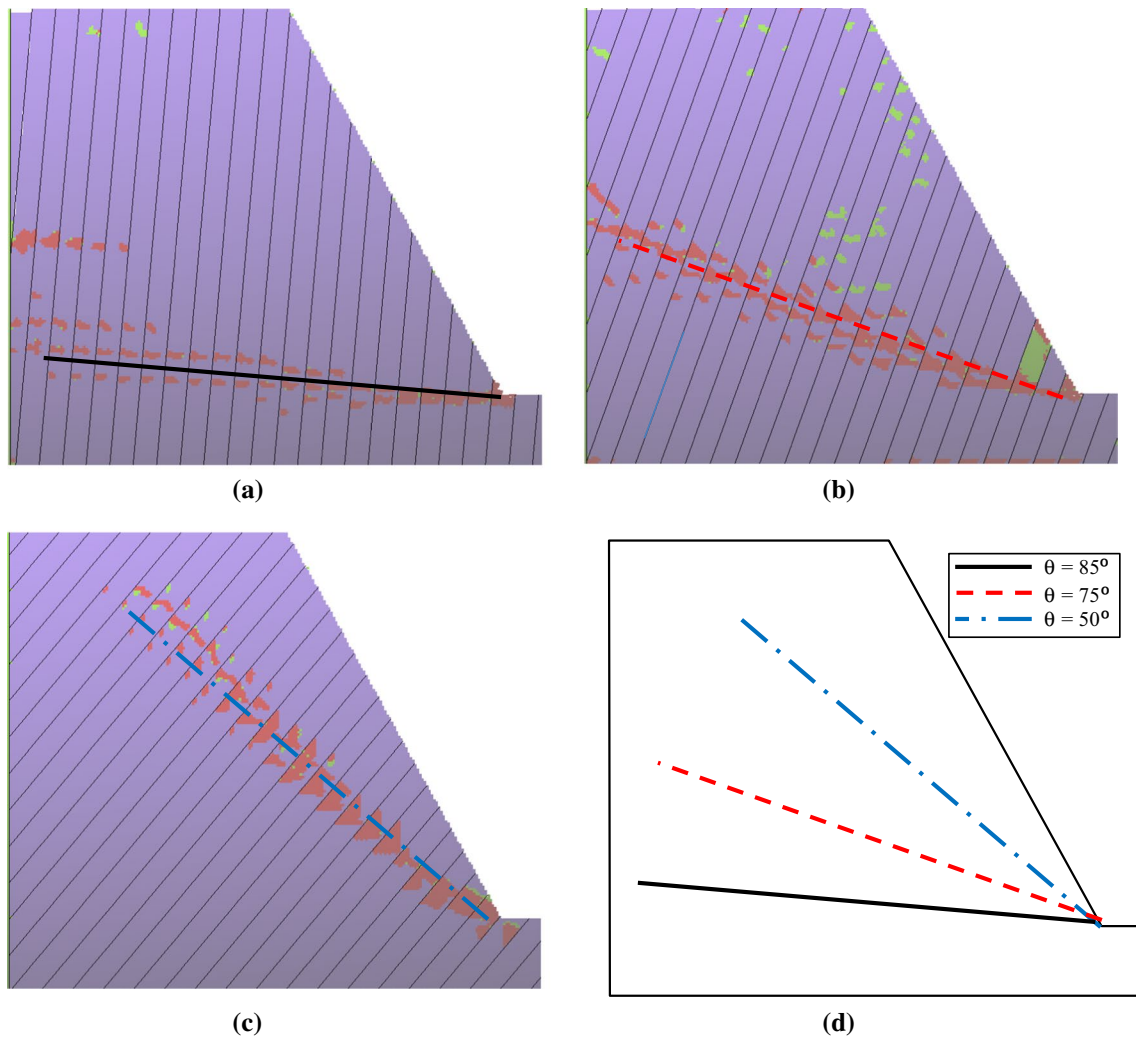


Fig. 20 Fracture surface of the jointed rock slope under different joint angles. **a** $\theta = 85^\circ$, **b** $\theta = 70^\circ$, **c** $\theta = 50^\circ$, **d** comparison

Acknowledgements The research was financially supported by the National Key Research and Development Programme of China (2016YFC0401905), National Natural Science Foundation of China (51379140), and the State Key Laboratory for Geomechanics and Deep Underground Engineering, CUMT (Grant No. SKLGDUEK1706).

References

- Adhikary DP, Guo H (2002) An orthotropic Cosserat elasto-plastic model for layered rocks. *Rock Mech Rock Eng* 35(3):161–170
- Adhikary DP, Dyskin AV, Jewell RJ, Stewart DP (1997) A study of the mechanism of flexural toppling failure of rock slopes. *Rock Mech Rock Eng* 30(2):75–93
- Alzoubi AK, Martin CD, Cruden DM (2010) Influence of tensile strength on toppling failure in centrifuge tests. *Int J Rock Mech Min Sci* 47:974–982
- Aydan O, Kawamoto T (1992) Stability of slopes and underground openings against flexural toppling and their stabilisation. *Rock Mech Rock Eng* 25(3):143–165
- Chen ZY, Gong WJ, Guowei MA, Wang J, Lei HE, Xing YC, Xing JY (2015) Comparisons between centrifuge and numerical modeling results for slope toppling failure. *Sci China Technol Sci* 58(9):1497–1508
- Cundall PA (1971) A computer model for simulating progressive large scale movements in blocky rock systems. In: *Proceedings of the international symposium on rock fracture, Nancy, October 1971. International Society for Rock Mechanics (ISRM)*, 1, paper no. II-8, pp 129–136
- Goodman RE, Bray JW (1976) Topping of rock slopes. *ASCE speciality conference on rock engineering for foundations and slopes, Boulder Colorado, vol 2*, pp 201–234
- Kazerani T, Zhao GF, Zhao J (2010) Dynamic fracturing simulation of brittle material using the distinct lattice spring method with a full rate-dependent cohesive law. *Rock Mech Rock Eng* 43(6):717–726
- Li LC, Tang CA, Zhu WC, Liang ZZ (2009) Numerical analysis of slope stability based on the gravity increase method. *Comput Geotech* 36:1246–1258
- Shi GH, Goodman RE (1985) Two dimensional discontinuous deformation analysis. *Int J Numer Anal Meth Geomech* 9(6):541–556
- Swan CC, Seo Y (1999) Limit state analysis of earthen slopes using dual continuum/FEM approaches. *Int J Numer Anal Methods Geomech* 23(12):1359–1371
- Zhang JH, Chen ZY, Wang XG (2007) Centrifuge modeling of rock slopes susceptible to block toppling. *Rock Mech Rock Eng* 40(4):363–382
- Zhang GX, Zhao Y, Peng XC (2010) Simulation of toppling failure of rock slope by numerical manifold method. *Int J Comput Methods* 7(01):167–189
- Zhao GF (2015) Further development of distinct lattice spring model for jointed rock masses. *Int J Rock Mech Min Sci* 78:79–90
- Zhao GF (2017) Developing a four-dimensional lattice spring model for mechanical responses of solids. *Comput Meth Appl Mech Eng* 315:881–895
- Zhao GF, Fang J, Zhao J (2011) A 3D distinct lattice spring model for elasticity and dynamic failure. *Int J Numer Anal Methods Geomech* 35:859–885
- Zhao GF, Fang J, Sun L, Zhao J (2013) Parallelization of the distinct lattice spring model. *Int J Numer Anal Methods Geomech* 37(1):51–74
- Zhao GF, Russell AR, Zhao X, Khalili N (2014a) Strain rate dependency of uniaxial tensile strength in gosford sandstone by the distinct lattice spring model with x-ray micro CT. *Int J Solids Struct* 51(7–8):1587–1600
- Zhao Y, Zhao GF, Jiang Y, Elsworth D, Huang Y (2014b) Effects of bedding on the dynamic indirect tensile strength of coal: laboratory experiments and numerical simulation. *Int J Coal Geology* 132:81–93
- Zienkiewicz OC, Humpheson C, Lewis RW (1975) Associated and nonassociated viscoplasticity in soil mechanics. *Géotechnique* 25(4):671–689